Zhu, Dongyang; Du, Jing; Peng, Zhongxiang; Wang, Jian; He, Xiang; Li, Gen; Ye, Long; Ling, Haifeng; Zhao, Meiting; Lin, Hongzhen; Ji, Deyang; Hu, Wenping

Metal–Organic Frameworks Coordination-Oriented Polymer Dielectrics for Neuromorphic Vision Sensors

Published in:
SmartMat

DOI:
10.1002/smm2.1322

Published: 01/02/2025

Document Version
Publisher's PDF, also known as Version of record

SmartMat

WILEY

SmartMat Open Access

RESEARCH ARTICLE OPEN ACCESS

Metal–Organic Frameworks Coordination-Oriented Polymer Dielectrics for Neuromorphic Vision Sensors

Dongyang Zhu[1] | Jing Du[1] | Zhongxiang Peng[2] | Jian Wang[3] | Xiang He[4] | Gen Li[5] | Long Ye[2] | Haifeng Ling[4] | Meiting Zhao[1] | Hongzhen Lin[3] | Deyang Ji[1,6,7] | Wenping Hu[6,7,8]

[1]Department of Chemistry, Tianjin Key Laboratory of Molecular Optoelectronic Sciences, Institute of Molecular Aggregation Science, Tianjin University, Tianjin, China | [2]School of Materials Science and Engineering, Tianjin University, Tianjin, China | [3]Suzhou Institute of Nano-Tech and Nano-Bionics Chinese Academy of Sciences, Suzhou, China | [4]State Key Laboratory of Organic Electronics and Information Displays & Institute of Advanced Materials, Nanjing University of Posts & Telecommunications, Nanjing, China | [5]Department of Chemical and Metallurgical Engineering, School of Chemical Engineering, Aalto UniversityEspoo, Espoo, Finland | [6]Key Laboratory of Organic Integrated Circuit, Ministry of Education, Tianjin University, Tianjin, China | [7]Collaborative Innovation Center of Chemical Science and Engineering, Tianjin University, Tianjin, China | [8]Department of Chemistry, Tianjin Key Laboratory of Molecular Optoelectronic Sciences, School of Science, Tianjin University, Tianjin, China

Correspondence: Haifeng Ling (iamhfling@njupt.edu.cn) | Meiting Zhao (mtzhao@tju.edu.cn) | Hongzhen Lin (hzlin2010@sinano.ac.cn) | Deyang Ji (jideyang@tju.edu.cn)

Received: 3 May 2024 | **Revised:** 16 May 2024 | **Accepted:** 17 May 2024

Funding: The study was supported by the National Key Research and Development Program of China (2021YFA0717900), National Natural Science Foundation of China (62004138, 52273190), and Beijing National Laboratory for Molecular Sciences (BNLMS202006).

Keywords: artificial synapse | interface engineering | metal–organic frameworks | organic phototransistors

ABSTRACT

Interface engineering based on polymer dielectrics shows great promise in organic field-effect transistors (OFETs)-based neuromorphic vision sensors (NeuVS). However, the highly disordered chain arrangement of polymer dielectrics often has a negative impact on the dynamic behavior of charge carriers, thereby affecting the sensing, memory, and computing performance of devices. To this end, we report an effective strategy to improve the orientation of polymer dielectrics by using a coordination combination of metal–organic frameworks (MOFs) and polymer. As a result, the coordination of MOFs with polymers improves the polarization of hydroxyl (−OH) and the resulting interfacial dipole could achieve an increase of photogenerated carriers in NeuVS with both higher mobility (above 20 $cm^2/(V \cdot s)$) and better optical figures of merit than devices without the coordination of MOFs. Furthermore, the new MOFs-polymer dielectric gives NeuVS devices temporal dynamics that enable better color extraction in static images. More importantly, in-sensor perception of moving objects was simulated, allowing postprocessing to produce over 95% action recognition accuracy. This attempt provides a new idea for the development of dielectric materials for highly sensitive light detection and visuomorphic computing.

1 | Introduction

With the increasing importance of artificial intelligence (AI) in many applications, a revolutionary device neuromorphic visual sensor (NeuVS) is proposed and rapidly developed, which mimics the visual system of living organisms and integrates "sensing, memory, and computing" functions in one device [1–4]. Organic field-effect transistors (OFETs) are considered to be a promising platform for NeuVS due to the physically separated control terminal (gate electrode) and the transduction terminals (source-drain electrodes), as well as the highly sensitive signal amplification [5, 6]. Besides, the use of OFET structures in NeuVS could endow these devices with the capabilities to modulate sensing, memory, and computing through

interface engineering and semiconductor selection, thus providing them with a broader development space [7–10]. Therefore, interfacial modulation using polymer dielectrics exhibits more possibilities for effectively functionalizing device interfaces [9, 11, 12], thanks to their advantages of diverse structural tunability, desirable mechanical flexibility, convenient solution processability, and excellent substrates compatibility, laying the foundation for low-cost and large-scale integrated devices [13–16]. However, the inherently disordered orientation and poor crystallinity of polymer usually have a negative impact on the dynamic behavior of charge transfer, injection, and storage, thereby affecting the sensing, memory, and computing performance of devices, greatly limiting their further development in NeuVS.

On the contrary, metal–organic frameworks (MOFs) are porous materials with high crystalline and precise arrangement of organic ligands and metal nods, but poor film-forming properties [17–23]. On this basis, in this work, we introduce MOFs into the polymer dielectric system, in which the metal nods of MOFs can coordinate with the specific functional groups in polymers, resulting in the improvement of the orientation and crystallinity of the polymer. Importantly, it is also found the polarization of hydroxyl (−OH) in this MOFs-polymer dielectric material is enhanced, thereby, the fabricated NeuVS has both high mobility of exceeding 20 $cm^2/(V \cdot s)$ and excellent optical figures of merit, which could be ascribed to the resulting interfacial dipole for an increase of carriers. Furthermore, the NeuVS devices demonstrated volatile photoresponses with temporal dynamics, including pulse-interval, pulse-intensity, pulse-duration, and pulse-number-dependent plasticity. Due to the dynamic behavior in the NeuVS device, color extraction in static images and the perception of moving objects were successfully simulated, providing a promising platform for artificial vision systems.

2 | Experimental Section

2.1 | Device Fabrication

The bottom-gate top-contact OFETs were prepared for the study. The ITO glass substrates used in the study were cleaned using deionized water, acetone, and isopropanol in that order and dried using nitrogen gas. The ITO surface was treated with O_2 plasma (50 W, 5 min). The plasma treatment was carried out using Diener Electronic GmbH + Co. KG (Germany). Afterward, PAA, PM1, and PM2 were spin-coated onto the treated ITO substrate at 3000 r/min. Subsequently, 20 nm C_{10}-DNTT was deposited by vacuum thermal evaporation at a rate of 0.05 Å/s. Finally, the 20 nm gold source and drain electrode was thermally evaporated through a shadow mask.

2.2 | Device Characterization

The morphology of the Zr-BTB and dielectric layers were recorded using a high-resolution field emission scanning electron microscope (Hitachi SU8010, Japan) and a field emission transmission electron microscope (Philips Tecnai G2 F20, The Netherlands) respectively. Surface topography of dielectric layers and semiconductors was recorded in percussion mode under atmospheric conditions using an atomic force microscope (Bruker Dimension ICON-PT, USA). The time-of-flight secondary-ion mass spectrometry (TOF-SIMS) data were collected from TOF-SIMS 5-100 to observe the 3D distribution and depth information of each species. The semiconductor crystalline structures were analyzed by 1D-XRD (MiniFlex 600) through scanning 2θ from 2° to 30° and 2D-GIWAXS at the 3 C beamline ($\lambda = 0.1230$ nm). The capacitance of the PAA, PM1, and PM2 was measured by Wuhan BALAB Technology Co. Ltd. using the BALAB DMS-500. The phototransistors were characterized in the air using a Keithley 2636B with different wavelengths, and power light applied using Zolix MLED4-3, HSX-UV 300 xenon light source, and an Omno 301 monochromator. The mobility was extracted from the saturation region by using the equation of $I_{DS} = \left(\frac{W}{2L}\right) C_i \mu (V_G - V_T)^2$. Sum frequency generation (SFG) spectrometer laser system was built by EKSPLA, operating at 50 Hz with a copropagating configuration (SINANO, China), and the pulse width was ≈25 ps. The visible wavelength was fixed at 532 nm, while the IR rhythm was tunable between 1000 and 4300 cm^{-1}. The incident angle was 60° for the visible beam and 55° for the IR beam. The SFG signal was collected at around 59.5° in the reflection geometry within a small range depending on the IR wave number (2800–3000 cm^{-1} in the experiment). The spectrum was recorded at 2 cm^{-1} addition per scan and was around more than 200 laser pulses per point.

The molecular dynamics simulations were performed using the Forcite module in Materials Studio. The model and parameter settings are described as follows.

The poly (amic acid) (PAA) polymer chain consisted of six PAA structural units. To simulate the aggregation behavior between polymer chains, six polymer chains were added to the simulation box. The Universal force field was employed to describe the interatomic interactions. The simulations were conducted under the NVT ensemble at a temperature of 273.15 K. A total simulation time of 1000 ps was employed with a time step of 1 fs. The charge distribution of the system was determined using the charge equilibration (QEq) method. The electrostatic interactions and van der Waals interactions were computed using the Ewald method. The temperature was controlled using the Nose method, which maintained a constant temperature throughout the simulation.

3 | Results and Discussion

3.1 | Preparation and Characterization of MOFs-Polymer Dielectric Layers

To achieve coordination binding between MOFs and polymers, a Zr-based MOF, Zr-BTB (BTB=benzene-1,3,5-tribenzoate) with available coordination sites for carboxylic acid and poly (amic acid) (PAA) with free acid groups were chosen, respectively. As shown in the structural formula in Figure 1A, the Zr_6 clusters in Zr-BTB coordinate with 6 BTB linkers to form 2D layered MOFs, and 6 other coordination sites of the Zr_6 clusters located above and below the layers are available for other acids (e.g., carboxylic acid on

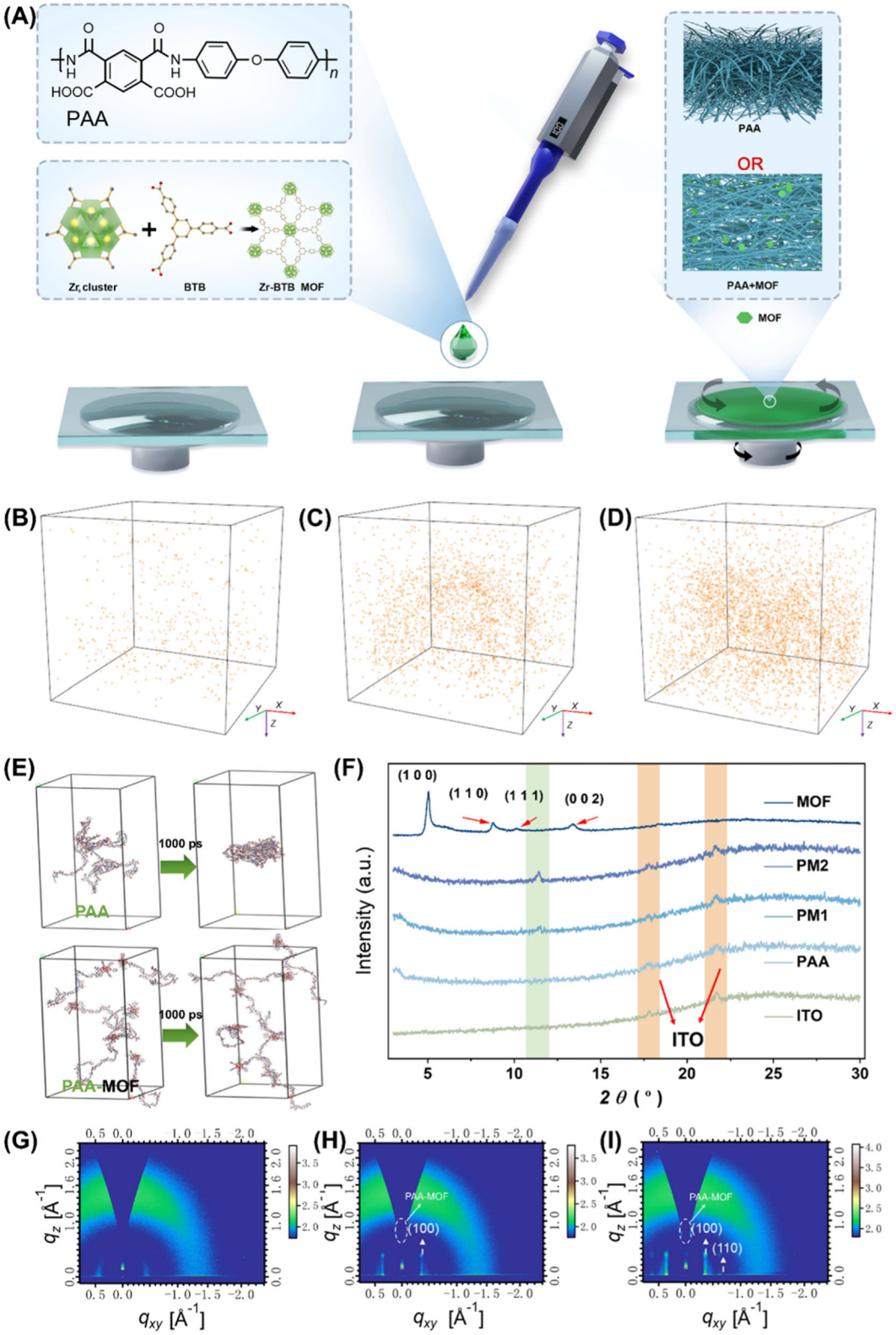

FIGURE 1 | Preparation and characterization of MOF-polymer dielectric layers. (A) Schematic diagram of spin coating to prepare PAA film or MOF-polymer composite film, the chemical structure of polymers PAA and MOF. Distribution of Zr contents within the three films of (B) PAA, (C) PM1, and (D) PM2. (E) Molecular dynamics simulation of PAA and PAA on MOF. (F) XRD patterns of ITO, PAA, PM1, PM2, and MOF. GIWAXS patterns of (G) PAA, (H) PM1, and (I) PM2. MOF, metal-organic framework; PAA, poly (amic acid).

PAA) [24, 25]. In addition, Zr-BTB also possesses advantages including simple preparation, high crystallinity, high thermal and chemical stability, and high mechanical strength [24, 26–28]. Zr-BTB was synthesized according to the previously reported method [29]. As shown in Supporting Information: Figure S1A, the obtained Zr-BTB are all sheet-like structures (~3 nm), and the low contrast of the corresponding transmission electron microscopy (TEM) images indicates the inherent ultrathin thickness of the nanosheets (Supporting Information: Figure S1B). And then, solutions are prepared by blending PAA with different masses (0, 0.37, and 0.73 mg/mL) of MOFs, which are further marked as PAA, PM1(PAA-MOF-1), and PM2 (PAA-MOF-2), respectively. As shown in Supporting Information: Figure S2, PM2 clearly has more Zr-BTB nanosheets than PM1. Subsequently, these three solutions are spin-coated (Figure 1A) onto ITO/Glass substrates to form uniform films as dielectric layers. The surface morphologies of the three dielectric layers: PAA, PM1, and PM2 were characterized by scanning electron microscope (SEM) (horizontal and tilted 45 degrees states) and atomic force microscopy (AFM). It can be clearly seen that the films based on PAA, PM1, and PM2 are uniform and smooth with a surface roughness of 0.53, 0.47, and 0.43 (Supporting Information: Figure S3), which demonstrates that the Zr-BTB nanosheets successfully blended into the polymers. Furthermore, the elemental distributions of Zr in these three different films were tested by time-of-flight secondary ion mass spectrometry (TOF-SIMS), and it was clearly observed that the even distribution of Zr contents in the films gradually increases with an increase in MOF amount (Figure 1B–D), indicating the uniform mixing of Zr-BTB and PAA. Besides, density functional theory (DFT) was used to show the molecular dynamics simulation of PAA and PAA-MOF systems. Without the coordination of MOF, it is observed that the intramolecular aggregation of the PAA molecule occurs first, followed by intermolecular aggregation (Supporting Information: Figure S4A,B), which is ascribed to the π–π conjugation and hydrogen bonding interaction between aromatic rings leading to the irregular aggregation in pure PAA system (Figure 1E). By contrast, the coordination of MOF with PAA would reduce the intramolecular and intermolecular interaction, and induce PAA molecular chains to reach an extended state (Supporting Information: Figure S4C,D) due to the larger mean square displacement of the PAA-MOF system than PAA system (Supporting Information: Figure S5), which would possibly induce the more orderly arrangement of polymer chains. The details of molecular dynamics simulation of PAA and PAA-MOF system are shown in Supporting Information: Video S1—4. Subsequently, to verify the successful coordination between Zr-BTB and PAA, X-ray diffraction (XRD) and grazing incidence wide-angle X-ray scattering (GIWAXS) are performed. As can be seen in Figure 1F, the XRD data of Zr-BTB has obvious spikes, which can be ascribed to the (100), (110), (111) (002) planes, respectively, indicating the good crystallinity of Zr-BTB MOF. Interestingly, after mixing PAA with Zr-BTB, a newly appeared sharp peak was observed, which was not a characteristic peak of Zr-BTB MOF and should be ascribed to the coordinated MOF-polymer dielectric materials, which demonstrated that the coordination between MOF and PAA could increase the ordering and crystallinity of the amorphous PAA polymer.

To verify the presence of Zr-BTB further experimentally and its effect on polymer ordering and crystallinity, GIWAXS tests were performed on PAA, PM1, and PM2. The GIWAXS patterns are shown in Figure 1F–H, and distinct MOF peaks are present in PM1 and PM2. By extracting the out-of-plane and in-plane one-dimensional curves from the GIWAXS data, the diffraction peaks of Zr-BTB (100) (110) can be clearly seen (Supporting Information: Figure S6A,B) [13, 30], which are consistent with the XRD data shown in Figure 1F. In addition, a new peak at around 0.78 $Å^{-1}$ was observed for PM1 and PM2 (Supporting Information: Figure S6A), matching well with the peaks at 11.4° in the XRD pattern (Figure 1F). Meanwhile, the molecular stacking spacing (d), full width at half maxima (FWHM), and coherence length (CL) of PAA, PM1, and PM2 can be obtained by fitting the out-of-plane diffraction peaks of the polymer (broad peaks around 1.46 $Å^{-1}$), and the data are summarized in Supporting Information: Table S1. It can be clearly concluded that the increasing coherence length could prove the improved ordering of polymer with the addition of Zr-BTB. With the GIWAXS data, the pole figures of polymer diffraction peaks around q of 1.46 Å can be extracted for analysis (Supporting Information: Figure S6C). The relative degree of crystallinity (r_{DOC}) is calculated as follows [31, 32]:

$$r_{DOC} \propto \int_{\omega_{min}}^{\frac{\pi}{2}} I(\omega)\sin(\omega)\mathrm{d}(\omega). \quad (1)$$

The calculated data are summarized in Supporting Information: Table S2, where the r_{DOC} of the polymer increases significantly with the addition of MOF. Therefore, the successful coordination between Zr-BTB and PAA could improve not only polymer ordering but also crystallinity.

3.2 | Preparation and Light Detection Properties of NeuVS Devices

For the application of NeuVS, as shown in Figure 2A, we prepared an OFET array with a bottom-gate top-contact device structure using the novel polymer-MOFs as the dielectric layer, 2,9-didecyldinaphtho[2,3-b:2,3-f] thieno[3,2-b] thiophene (C_{10}-DNTT) as the channel semiconductor, and Au as the source/drain electrodes. Figure 2B shows an optical photograph of the transistor arrays with 48 devices. Here, we also introduce the bare PAA dielectric without MOF coordination for comparison. Firstly, the surface morphologies of the C_{10}-DNTT grown on these three kinds of dielectric layers were characterized (Supporting Information: Figure S7) and there is no significant difference in the morphological growth of the semiconductors. However, the GIWAXS data (Figure 2C–E and Supporting Information: Table S3) demonstrated that the moderate addition of MOF content could increase the ordering of C_{10}-DNTT on the dielectric layer due to the increasing coherence length (CL). When more MOF content was added into the PAA, not only the stacking spacing of semiconductor molecules was increased but also the coherence length was reduced resulting in the decrease of the ordering of C_{10}-DNTT on dielectric. As a result, the mobility of the NeuVS devices was enhanced with the value exceeding 20 $cm^2/(V \cdot s)$ with the moderate addition of MOF content, but excessive MOF content would decrease the performance of the devices (Table 1). The representative transfer and output curves of the NeuVS devices with the PAA, PM1, and PM2 as dielectric layers are shown in Supporting

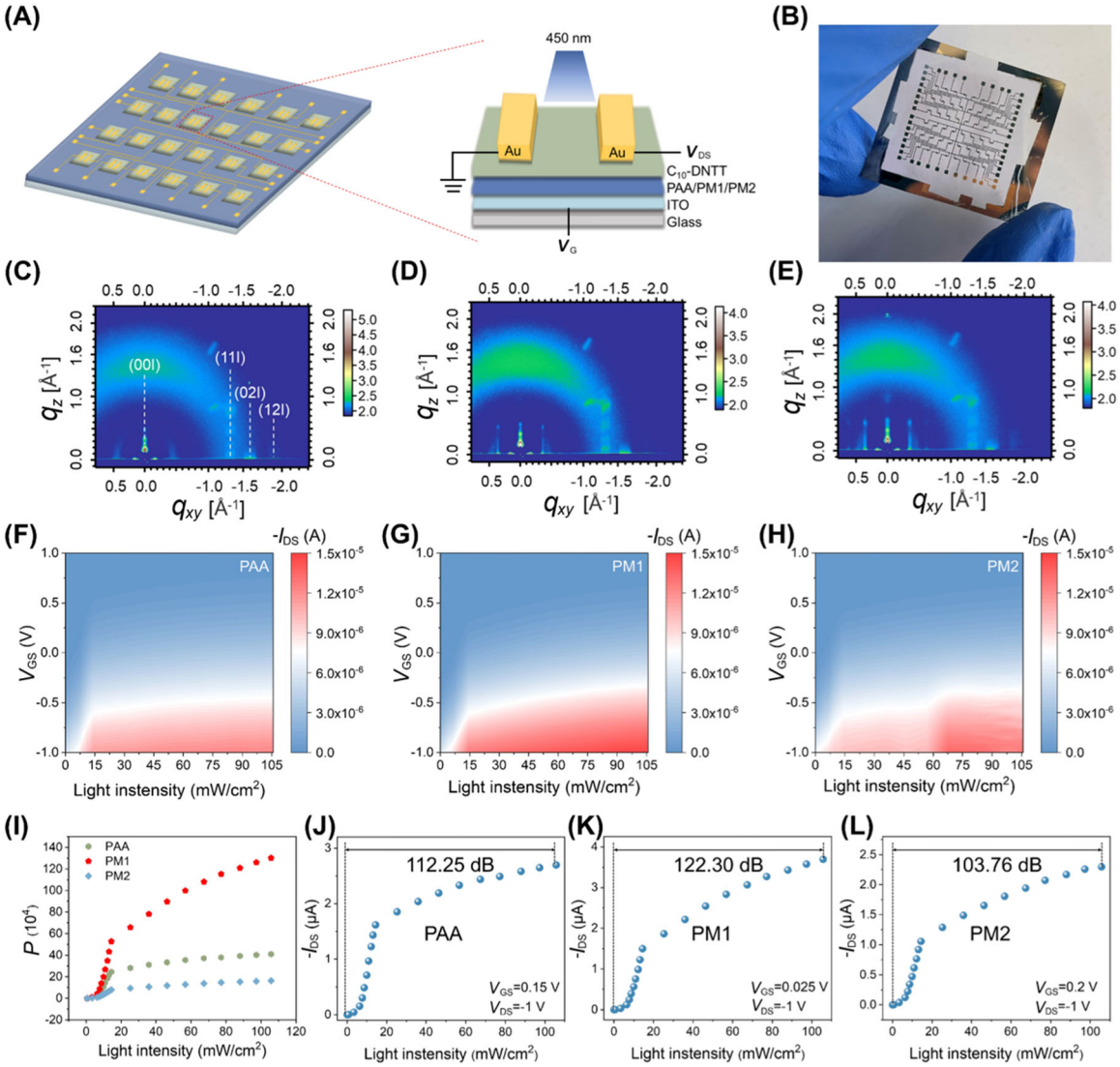

FIGURE 2 | Device structure and light detection properties of NeuVS devices. (A) Schematic diagram of organic phototransistor array and single device structure. (B) Organic phototransistor array optical diagram. GIWAXS data of C_{10}-DNTT on (C) PAA, (D) PM1, and (E) PM2. Photocurrent distribution of OPTs based on (F) PAA, (G) PM1, and (H) PM2 at different light intensities. (I) Plot of the maximum *P*-value of PM1-based OPTs as a function of light intensity. Dynamic response range of OPTs based on (J) PAA, (K) PM1, and (L) PM2. GIWAXS, grazing incidence wide angle X-ray scattering; NeuVS, neuromorphic visual sensor; PAA, poly (amic acid).

TABLE 1 | Relevant key parameters obtained from testing and statistics for five NeuVS devices.

	V_{th} (V)	I_{on}/I_{off} (10^5)	S (V/dec)	C_i (nF/cm^2)	μ (cm^2/(V · s))
PAA	−0.145 ± 0.007	5.87 ± 0.6	−0.125 ± 0.007	65.99 ± 9.93	11.82 ± 0.68
PM1	−0.285 ± 0.007	15.75 ± 0.07	−0.128 ± 0.004	82.71 ± 11.63	20.62 ± 0.8
PM2	−0.15 ± 0.014	3.82 ± 0.3	−0.135 ± 0.007	95.48 ± 4.85	16.66 ± 0.84

Abbreviation: NeuVS, neuromorphic visual sensor; PAA, poly (amic acid).

Information: Figure S8, while the capacitance and device mobility of PAA, PM1, and PM2 at different frequencies are shown in Supporting Information: Figure S9. All the fabricated NeuVS devices could work at a low operating voltage of −1 V with an on/off ratio above 10^5.

Subsequently, the photoresponse performance of these three kinds of NeuVS devices under 450 nm monochromatic light was further tested. About nineteen different illumination densities from 0.61 to 105.73 mW/cm^2 were radiated onto the devices with the corresponding transfer curves shown in Figure 2F–H and Supporting Information: Figure S10. All the NeuVS devices exhibited positive photoresponse not only to a weak light density of 0.61 mW/cm^2 but also to a strong light density of 105.73 mW/cm^2. However, the coordination between MOF and PAA has a different influence on the optical figures of merit

based on these three kinds of dielectrics. As shown in Figure 2I and Supporting Information: Figure S11, the value of calculated photosensitivity (P) as a function of the source-drain voltage (V_{GS}) demonstrated that the higher photoresponse was detected from the device using PM1 as a dielectric layer with the best value exceeding 10^6. In addition, the dynamic response ranges could also be calculated based on the following equation:

$$\text{Dynamic range} = 20 \log (I_{\text{illumination}}/I_{\text{dark}}). \quad (2)$$

where $I_{\text{illumination}}$ is the photoresponse current and I_{dark} is the dark current. As a result, the NeuVS device using PM1 as the dielectric layer achieved a higher gain of 122.3 dB (Figure 2K) compared with those based on PAA (Figure 2J) and PM2 (Figure 2L) dielectric layers, which indicated the wider and more discriminative light intensity distribution range in PM1-based devices. Besides, the photoresponsivity (R) and detectivity (D^*) are another two key parameters to evaluate the performance of phototransistor-based NeuVS devices. From the values in Supporting Information: Figure S12, it can be concluded that PM1-based devices showed a stronger ability to convert light into electric current and were more powerful for detecting incident light signals than the PAA-based and PM2-based devices. It is noteworthy that a moderate amount of MOF in PM1 could improve the device's performance; however, the excessive amount of MOF in PM2 would reduce the optical figures of merit. To further investigate the optimal ratio of MOF more accurately, another two systems with two kinds of MOF contents, PM0.5 and PM3, were added for data statistics and comparison as shown in Supporting Information: Figure S13 and the results also verify the optimum MOF content in PM1-based device.

To further investigate the possible mechanism between the MOF coordination and device performance, we first carried out the test to exclude the effect of metal ions in MOF by preparing the devices using the dielectrics with the blending PAA and equal amounts of Zr clusters. Here, we added $ZrOC_{l2}$-$8H_2O$ and $Zr_6(C_6H_5COOH)_{12}$ clusters into PAA, marked as PZ1 and PZ2 insulators, respectively. The fabricated transistors showed the typical transfer and output curves (Supporting Information: Figure S14) and their photoresponse behaviors to 450 nm monochromatic light with different illumination densities were also measured (Supporting Information: Figure S15). It was found that the addition of Zr species could decrease the device performance (Supporting Information: Figure S16), which demonstrated that metal clusters in MOF did not contribute to the photoelectrical characteristics.

Subsequently, sum frequency generation vibrational spectroscopy (SFG-VS) was introduced to follow the interfacial changes [33]. As a second-order nonlinear optic technique, SFG-VS possesses interface selectivity and is highly sensitive to the orientation orderliness of the interfacial molecules/groups. As seen in Figure 3A, several peaks in the 2800–3000 cm^{-1} region can be assigned to the stretching vibrations and Fermi resonances of the methyne (−CH) and methylene ($-CH_2$) groups of PAA, while those at around 2720 and 2780 cm^{-1} are most likely originated from the vibration modes of the organic moiety of MOF [34]. The PAA orderliness is greatly enhanced by mixing with MOF, as suggested by the increased SFG signals at the $-CH_x$ stretching region. The lack of $-CH_2$ Fermi resonance at 2900–2920 cm^{-1} for PM1 without the semiconductor (C_{10}-DNTT) layer indicates a low degree of intermolecular interaction between the PAA chains in PM1 [35–37]. These results mean that the alkyl chains are less aggregated while more orderly oriented in PM1, which in turn leads to less interchain coupling and weaker hydrogen bonding and hence freer −OH upon introducing the semiconductors, as evidenced by the red-shifted $-CH_x$ band and blue-shifted −OH vibrations for the PM1 + C_{10}-DNTT sample in comparison to the other two. The "turn-on" behavior of the −OH signals upon the introduction of the semiconductor layer suggests that the orientation of −OH is mostly induced by the built-in potential at the dielectric/semiconductor interface, rather than an inherent property of the dielectric itself. The presence of a moderate amount of MOF in PM1 reduces the intermolecular hydrogen bonding to the highest extent, allowing the relatively free −OH to form a maximum mutual isolated dispersion from the alkyl portion (Figure 3B). And this isolated dispersion makes the −OH more easily polarized and generates interfacial dipole, which is favorable to the generation of photogenerated carriers. Since the MOF itself also contains −COOH groups, the excess of MOF in PM2 introduces more −OH to participate in the reformation of hydrogen bonding, which weakens the orientation polarizability of −OH and reduces the interfacial dipole, limiting the production of photogenerated carriers (Figure 3B) [38–40].

The above experiments demonstrated that the incorporation of an appropriate amount of Zr-BTB in PAA can achieve the improvement of optoelectronic performance. However, considering the possible influence of the MOF size, thicker Zr-BTB nanosheet (marked as Zr-BTB-T1 (~15 nm) and Zr-BTB-T2 (~40 nm), shown in Supporting Information: Figure S17A,B) was synthesized and prepared into transistor devices labeled PM-T1 and PM-T2, respectively, and the optoelectronic properties of PM-T1-based and PM-T2-based devices were tested and compared with those of PM1-based devices, and the results are shown in Supporting Information: Figure S18. It is evident that the increase in thickness has a significant negative effect on the performance of the devices and the photoresponsive performance decreases with the increase in the thickness of the Zr-BTB nanosheets. To verify whether PAA and Zr-BTB are unique, other types of MOF with different crystal structures and morphology were studied. Firstly, MOF-545 ($Zr_6O_8(H_2O)_8$(TCPP-$H_2)_2$, the chemical formulae shown in Supporting Information: Figure S17E) with different particle sizes and rod-like morphologies, labeled MOF-545-T1 (~30 × 50 nm) and MOF-545-T2 (~15 × 25 nm) (Supporting Information: Figure S17C,D), were synthesized, and then MOF-545-T1 and MOF-545-T2 were added in PAA solution labeled as PT1 and PT2, respectively [41, 42]. Finally, the photoelectric properties of PT1- and PT2-based devices were tested, and the results are displayed in Supporting Information: Figure S19. The addition of a moderate amount of MOF-545 indeed improves the device's performance, and the size of the MOF-545 also has an impact on the performance of the device. Subsequently, another two polymers, polyacrylic acid (PAA) and polyacrylonitrile (PAN) (the chemical formulae shown in Supporting Information: Figure S17F,G), were chosen to be combined with Zr-BTB, respectively. Different proportions of Zr-BTB were added to the PAA solution labeled aM1 and aM2. Moreover, aM1- and aM2-based transistor devices were

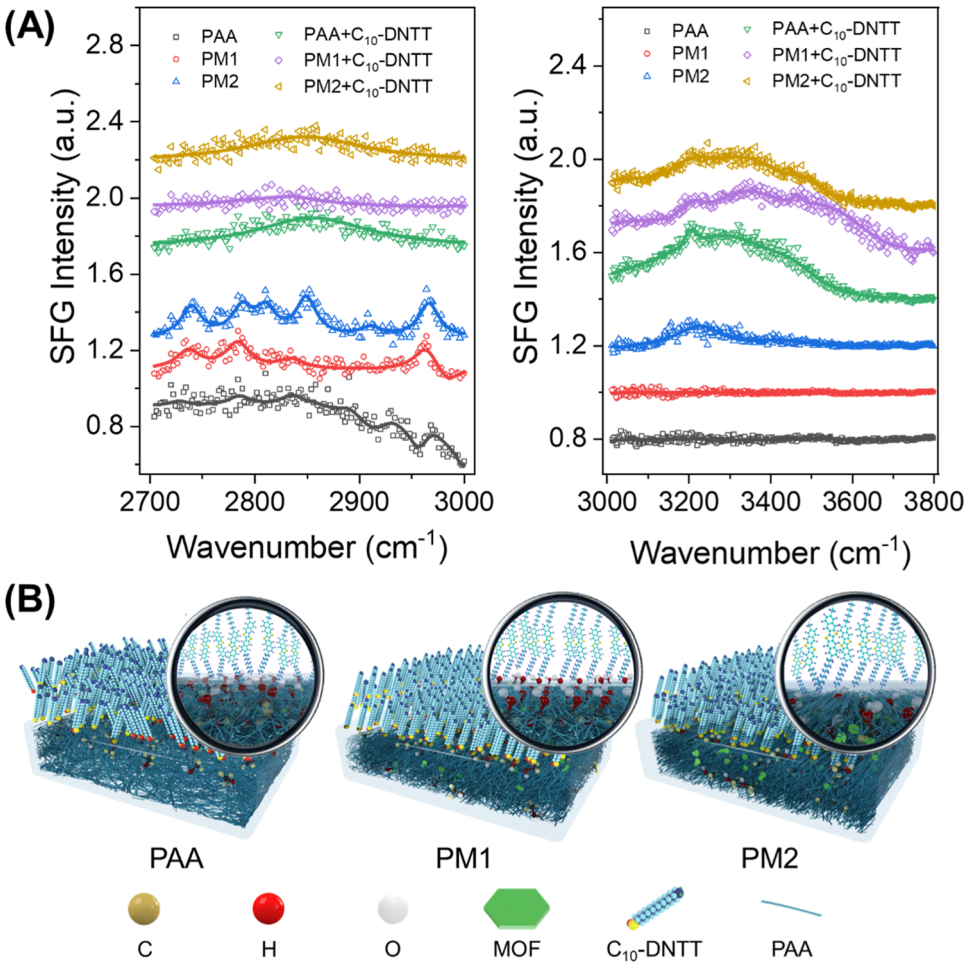

FIGURE 3 | The mechanism between MOF alignment and device performance. (A) SFG spectra, collected with ssp configuration, at PAA, PM1, and PM2 surfaces, and the corresponding dielectric/C_{10}-DNTT interfaces in the CH and OH vibration regions. (B) Interface mechanism diagram. C_{10}-DNTT, 2,9-didecyldinaphtho[2,3-b:2,3-f] thieno[3,2-b] thiophene; MOF, metal-organic framework; PAA, poly (amic acid).

tested, and the results are shown in Supporting Information: Figure S20. The results are the same as when using polymer PAA, where a moderate amount of MOF improves the photoresponsive performance, while an excessive amount of MOF degrades the photoresponsive performance. Subsequently, different ratios of Zr-BTB were added to the PAN solution, labeled as NM1 and NM2, and the results of the testing of the devices based on this construction are shown in Supporting Information: Figure S21. Zr-BTB addition has a significant negative effect on the optoelectronic performance of the devices, and the photoresponse decreases more as the amount of Zr-BTB increases. Therefore, the coordination between the MOF and carboxyl groups plays an important role in modulating the optoelectronic properties of devices.

3.3 | Temporal Behavior of NeuVS Devices

The human brain is a highly efficient biological computing system in which synapses are the basic units responsible for information learning, preprocessing, and storage [43, 44]. After studying the MOF-polymer dielectric-based NeuVS device with light sensing functions, we further investigate this device to simulate the biological synaptic function by using the optimized ITO/PM1/C_{10}-DNTT/Au structure. Figure 4A shows the biological synaptic structure between two adjacent neurons and the analogous OFET structure schematically. Neurons generate chemical and electrical signals by sensing external information, and presynaptic neurons release neurotransmitters that act on the corresponding receptors in the postsynaptic membrane to trigger postsynaptic signals. In the NeuVS devices, 450 nm monochromatic light was used as externally applied light stimuli to trigger the excitatory postsynaptic currents (EPSC) behavior in the form of channel current (I_{DS}).

In Figure 4B, the EPSC behaviors for the PM1-based NeuVS device under a 450 nm monochromatic light pulse are shown with a PAA-based device used for comparison. Under light illumination (450 nm, 0.61 mW/cm^2, 1 s), the EPSCs of both NeuVS devices increased dramatically and the PM1-based device had a higher peak value of EPSC response due to its high mobility. After the light illumination, the EPSCs are immediately reduced to lower values due to charges released from the shallow trapping sites, resulting in volatile memory or short-term plasticity (STP). The charge trapping capability of each device was evaluated by an exponential relationship with a time-decay constant (t_0; Supporting Information: Figure S22). The fitted PAA-based device had a relaxation time of $t_0 = 3.9$ s,

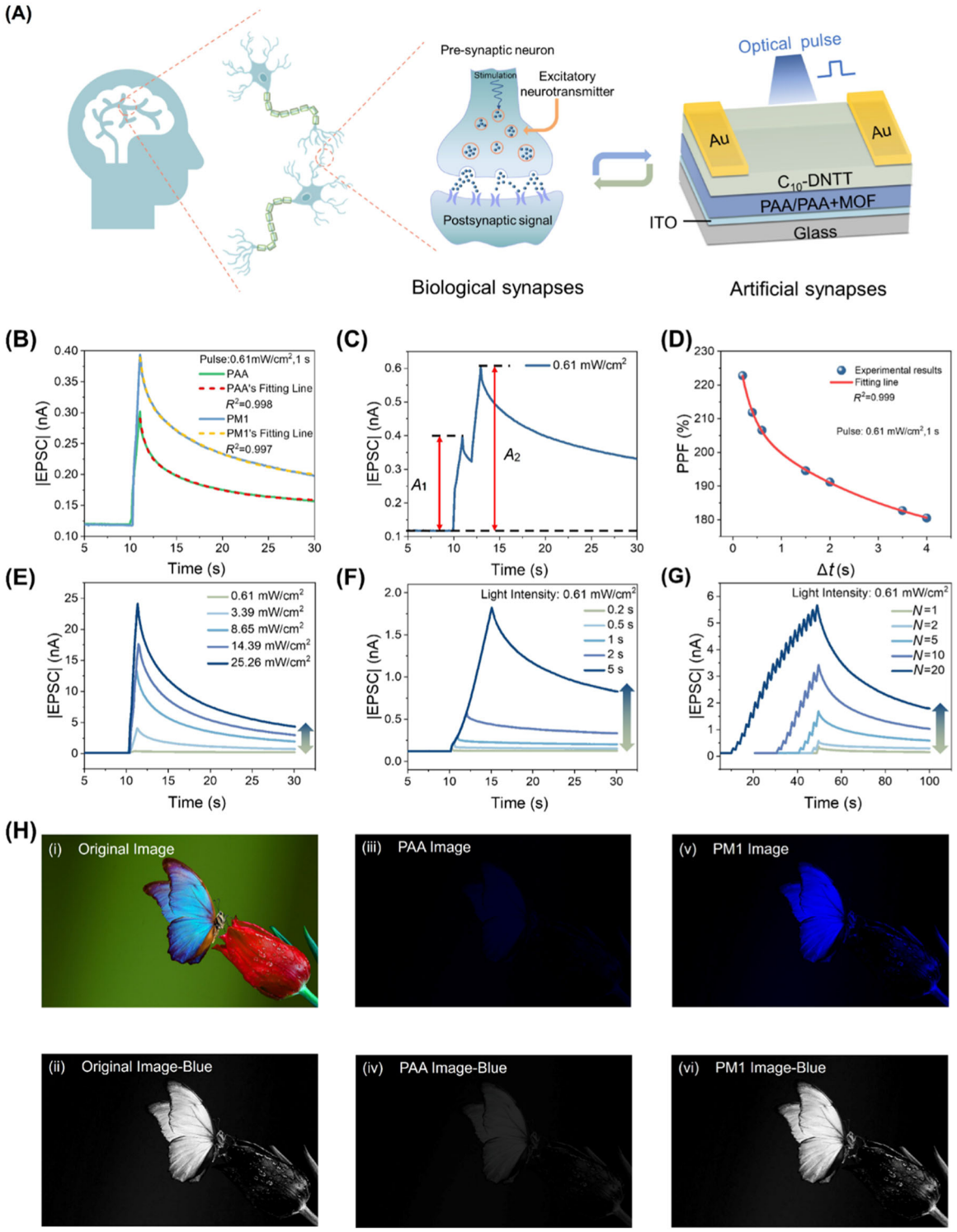

FIGURE 4 | Temporal behaviors of NeuVS. (A) Schematic diagram of neural signal transmission at biological synapses in neurons in the human brain and synaptic OFET device structure. (B) EPSC triggered by presynaptic light pulses (450 nm, 0.61 mW/cm^2, 1 s) in NeuVS devices with PAA (green line) and PM1 (blue line) as dielectric layers, respectively. The yellow and red lines fit the postsynaptic current decay lifetime of the two devices, respectively. (C) EPSCs in the PM1 NeuVS are triggered by a pair of optical pulses (450 nm, 0.61 mW/cm^2, 1 s) with an interval of 1 s. (D) PPF index as the function of optical pulse interval (Δt) with a light intensity of 0.61 mW/cm^2 and a pulse width of 1 s. The red solid line shows an exponential function. Tuning the time scale of STP by changing the (E) intensity, (F) duration, and (G) number of optical pulses. All the measurements of synaptic behaviors were performed at $V_{DS} = -0.2$ V and $V_{GS} = -0.1$ V. (H) (i) Original image with RGB components for color extraction. (ii) The blue component of the original image. The actual image of the theoretical output image of the (iii) PAA-based and (v) PM1-based devices obtained from simulation, the synaptic weight is the optimal weight. Blue components of the theoretical output images of the (iv) PAA- and (vi) PM1-based devices obtained from the simulation. EPSC, excitatory postsynaptic currents; NeuVS, neuromorphic visual sensor; OFET, organic field-effect transistors; PAA, poly (amic acid); PPF, pair-pulse facilitation; STP, short-term plasticity.

while the PM1-based device had $t_0 = 5.3$ s. In the human brain, the time scale of STP is basically a few milliseconds to a few minutes [45, 46]. PM1-based devices had a larger relaxation time, indicating the stronger charge trapping capability of PM1 dielectric due to the interfacial dipole [47].

In biological systems, pair-pulse facilitation (PPF) plays an important role in decoding temporal information. The PPF effect of two consecutive pulses at an interval time (Δt) of 1 s for the PM1-based device is presented in Figure 4C. The electrons generated by the first light pulse are retained at the interface until the next pulse appears to achieve current accumulation, thus it can be clearly seen that the peak value of EPSC induced by the second light pulse is significantly larger than that induced by the first light pulse, achieving a facilitation process. To further evaluate the PPF characteristics, the PPF index is adopted using the following equation:

$$\mathrm{PPF} = \frac{A_2}{A_1} \times 100\% \tag{3}$$

where A_1 and A_2 are the peak currents of the EPSC induced by the first and second light pulses, respectively. As shown in Figure 4D and Supporting Information: Figure S23A, the PM1-based device achieved a maximum PPF value of 223%, while the PAA-based device of 182%, indicating that the temporal correlations between the interconnected neurons were stronger in the PM1-based NeuVS device.

To get additional insights into the temporal dynamics of the NeuVS device, diversified photo-modulation EPSCs were further investigated. Figure 4E shows the EPSC changes triggered by PM1-based devices under different intensities of light pulses. As the light intensity increased from 0.61 mW/cm^2 to 25.26 mW/cm^2, the peak value of EPSC increased from 0.39 nA to 24.14 nA. The EPSC evoked by stronger light pulses took longer to decay, showing that the time scale of STP was improved with increasing light intensity. This tuning can also be achieved by adequate training, including pulse duration (Figure 4F) and number of pulses (Figure 4G), and so forth. For PM1 devices, the t_0 time resolution range was 0.06 to 16.6 s. The ability of NeuVS devices to tune the t_0 enables machine vision tasks to be processed. Although the PAA-based device could also exhibit the turning of time to decay, as shown in Supporting Information: Figure S23B–D, the comparison showed that the PM1-based device had a higher peak value of EPSC after training, indicating a more outstanding performance in terms of information processing ability. Moreover, this short-term property ensures that the device array can properly retain the spatiotemporal signal, and has the potential to detect the trajectory of objects.

One of the advantages of artificial synaptic devices is that it operates with low energy consumption. Both PAA- and PM1-based synaptic transistor devices can operate normally at ultra-low operating voltages of 1 mV, as shown in Supporting Information: Figure S24. The energy consumption of the NeuVS device in a single synaptic event can be calculated by $I_{peak} \times V \times t$, where I_{peak} refers to the peak value of the EPSC, V is the operating voltage, and t represents the pulse duration. When a 0.1 s pulse is applied to the PAA and PM1-based devices, respectively, the energy consumption of the synaptic device is 1.28 fJ and 5.5 fJ, which is much lower than the energy consumption of conventional CMOS and achieves an energy consumption comparable to that of biological synapses (1–10 fJ) [48, 49]. The above results demonstrate that NeuVS based on a novel polymer-MOF dielectric layer has obvious performance advantages over other optical neural systems (Supporting Information: Table S4) and shows potential for intelligent machine vision.

3.4 | Color Extraction in Static Image

In neural signal transmission, STP plays a significant role in filtering redundant information and extracting efficacious information from the original optical information. Based on the strong absorption of C_{10}-DNTT for blue-light-signals detection around 450 nm and the weak absorption for green light at 515 nm and red light at 690 nm, the function of color extraction could be implemented using the NeuVS array. The corresponding output color information was presented by using different EPSC states corresponding to different pulse numbers (1, 2, 5, and 10). The peak EPSC of the PAA- and PM1-based devices were first compared for different numbers of pulsed light stimuli at 450, 515, and 690 nm light, as shown in Supporting Information: Figure S25. The PM1-based device has a significantly higher response than the PAA-based device, especially under 450 nm light stimuli. That is when the main part of the signal is mainly composed of 450 nm radiation, the device's response to signals in the longer-wavelength parts of the environment is negligible. The original image shown in Figure 4H(i) was extracted as R, G, and B components as shown in Figure 4H(ii) and Supporting Information: Figure S26A,B, and then blue color extraction was performed using PAA- and PM1-based devices, respectively. A detailed explanation is given in Supporting Information: Note S1. The overall and different color component output images of the PAA- and PM1-based devices are shown in Figure 4H(iii)–(vi) and Supporting Information: Figure S26C–F, respectively. The PM1-based device is significantly better at extracting blue butterfly than the PAA-based device. The dependence of color contrast on the number of light pulses is shown in Supporting Information: Figure S27. With the increasing number of pulses, the contrast between the blue features and the other features can be enhanced, and the target of butterfly gradually becomes clearer. These results demonstrate that PM1-based devices can effectively distinguish blue color information from the original color image.

3.5 | Trajectory Detection and Recognition for Motion Objects

In addition to color extraction for static images, the designed PM1-based NeuVS was used to classify the motion directions (Figure 5A). A customized data set including four types of real-world motion (moving down, up, right, and left) was developed for vision system training and recognition. Simulation of a 36×36 sensor array can feed these images into a tiny artificial neural network, to simulate the relative motion trajectories of

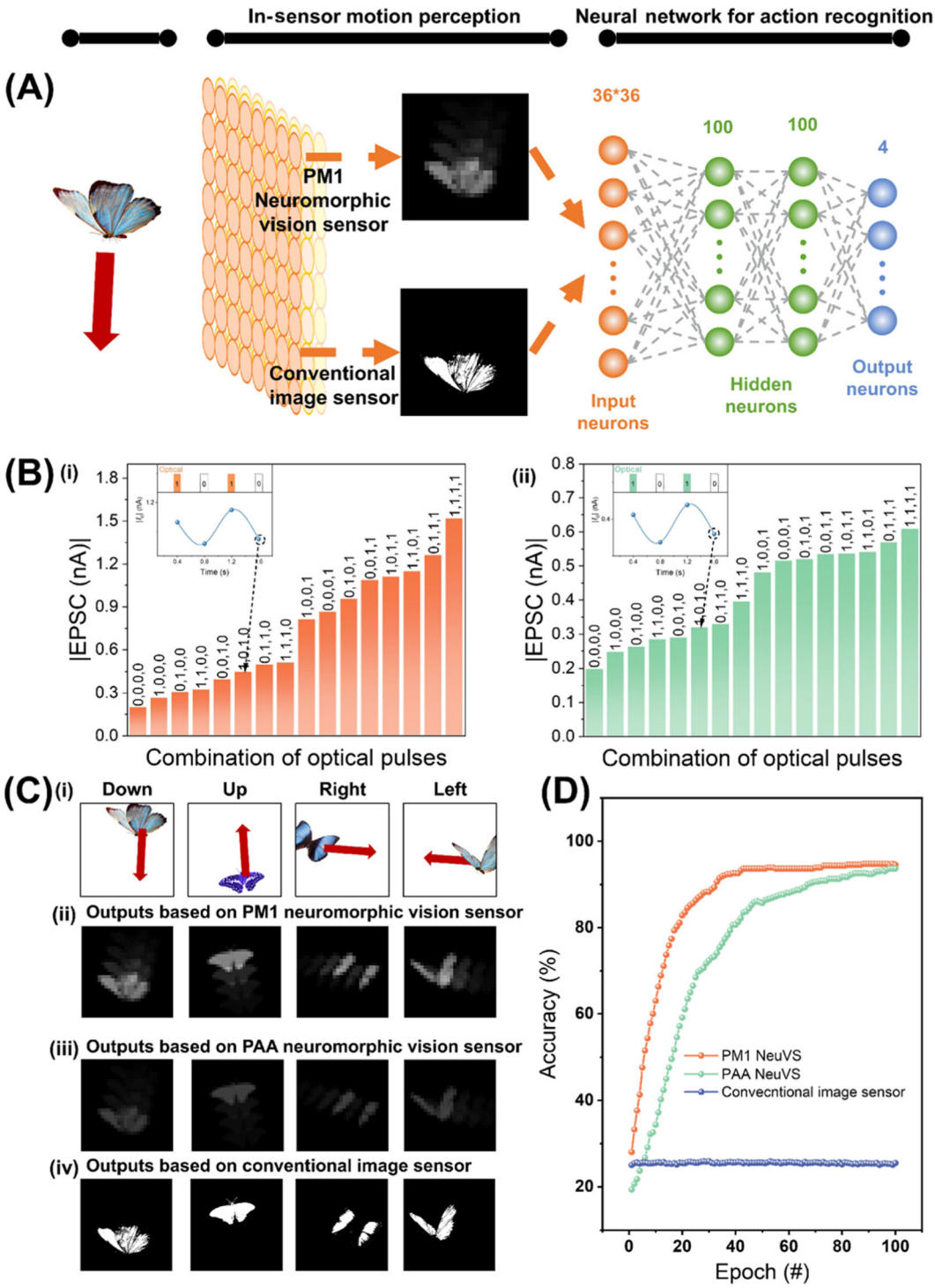

FIGURE 5 | Action recognition based on NeuVS. (A) A tiny neural network for action recognition with PM1-based NeuVS and conventional image sensor. NeuVS can output spatiotemporal frames, while conventional image sensors output only spatial frames. (B) Responses to four-bit light stimulation. The inset shows the encoding process for '1010' stimulation, where '1' and '0' represent 2.04 mW/cm^2 light illumination and dark conditions, respectively, with a light pulse duration of 200 ms and a duty cycle of 50%. (C) (i) Typical down, up, right, and left motions, (ii) the outputs from the PAA-based NeuVS, (iii) the outputs from the PM1-based NeuVS, and (iv) the outputs from a conventional image sensor. (D) The action recognition accuracy of PAA-based NeuVS, PM1-based NeuVS, and conventional image sensor. NeuVS, neuromorphic visual sensor; PAA, poly (amic acid).

birds or other predators seriously pursuing insects such as butterflies. The NeuVS can compress the spatiotemporal information of a sequence of frames by reducing background interference. In contrast, conventional image sensors output frames with only the spatial information.

The inset in Figure 5B shows the response process of the device to optical pulse encoding. The digits '1' and '0' represent 2.04 mW/cm^2 light illumination and dark conditions under conditions of the $V_{DS} = 0.2$ V, and $V_{GS} = 0.1$ V, and the optical pulse has a duration of 200 ms with a duty cycle of 50%.

Figure 5B shows the exported EPSC under four light pulses (16 combinations), revealing distinctive responses to the different four-frame actions that enable encoding processes. The EPSC is greatly dependent on the sequence of light stimulation. The superposition of the frames obtained with the NeuVS array can consolidate the spatiotemporal motion information through the distinctive level of the EPSCs.

Figure 5C(i) depicted the relative motion trajectories of butterfly as perceived by predators and frames with compressive temporal states output from the simulated array of the described NeuVS with PM1 (Figure 5C(ii)) and PAA (Figure 5C (iii)), respectively. The compressive frames clearly show the contour of the trajectory, which allows easy motion recognition. Figure 5D shows the recognition accuracy of the artificial neural networks with NeuVS and conventional image sensors during the training process. The accuracy of action recognition with NeuVS reached 95% after about 40 (PM1) and 100 (PAA) training rounds, much higher than that achieved with conventional image sensors (~25%).

4 | Conclusion

In summary, we reported a relatively ordered new polymer dielectric layer system PM1 by the coordination combination between PAA and 2D layered MOFs, and NeuVS devices were prepared based on the above dielectric layer. Benefiting from the coordination between 2D layered MOFs and PAA, the orderliness of the polymer was improved, and high crystallinity was achieved due to a higher density of metal centers with vacant coordination positions available to interact with the polymer. Meanwhile, the addition of a small amount of MOFs maximizes the impact on the organization of the polymer blend, improves the polarization of −OH, increases the interfacial dipole, and facilitates the generation of photogenerated carriers, realizing a short-term photoresponse. Owing to this dynamic behavior, the MOF-polymer dielectric-based NeuVS device can not only extract the blue color in static images but also encode sequentially temporal information and display trajectory contours, thereby enabling motion perception with a recognition accuracy of over 95%. These results show that the novel polymer-MOF dielectric layer provides a unique potential for neuromorphic vision sensors.

Acknowledgments

The authors are grateful to the National Key Research and Development Program of China (2021YFA0717900), National Natural Science Foundation of China (62004138, 52273190), and Beijing National Laboratory for Molecular Sciences (BNLMS202006).

Conflicts of Interest

The authors declare no conflicts of interest.

Data Availability Statement

The data that supports the findings of this study are available in the supplementary material of this article.

Code Availability Statement

The code used for the simulation is available from the corresponding author with detailed explanations upon reasonable request.

References

1. G. Indiveri and R. Douglas, "Neuromorphic Vision Sensors," *Science* 288, no. 5469 (2000): 1189–1190.

2. F. Zhou, Z. Zhou, J. Chen, et al., "Optoelectronic Resistive Random Access Memory for Neuromorphic Vision Sensors," *Nature Nanotechnology* 14, no. 8 (2019): 776–782.

3. S. Gao, G. Liu, H. Yang, et al., "An Oxide Schottky Junction Artificial Optoelectronic Synapse," *ACS Nano* 13, no. 2 (2019): 2634–2642.

4. Y. Xu, G. Zhang, W. Liu, et al., "Flexible Multiterminal Photoelectronic Neurotransistors Based on Self-Assembled Rubber Semiconductors for Spatiotemporal Information Processing," *SmartMat* 4, no. 2 (2023): e1162.

5. Z. He, H. Shen, D. Ye, et al., "An Organic Transistor With Light Intensity-Dependent Active Photoadaptation," *Nature Electronics* 4, no. 7 (2021): 522–529.

6. H. Shim, F. Ershad, S. Patel, et al., "An Elastic and Reconfigurable Synaptic Transistor Based on a Stretchable Bilayer Semiconductor," *Nature Electronics* 5, no. 10 (2022): 660–671.

7. A. Pierre, A. Gaikwad, and A. C. Arias, "Charge-Integrating Organic Heterojunction Phototransistors for Wide-Dynamic-Range Image Sensors," *Nature Photonics* 11, no. 3 (2017): 193–199.

8. H. Shen, Z. He, W. Jin, et al., "Mimicking Sensory Adaptation With Dielectric Engineered Organic Transistors," *Advanced Materials* 31, no. 48 (2019): 1905018.

9. Y. Zhao, S. Haseena, M. K. Ravva, et al., "Side Chain Engineering Enhances the High-Temperature Resilience and Ambient Stability of Organic Synaptic Transistors for Neuromorphic Applications," *Nano Energy* 104 (2022): 107985.

10. Y. Ni, L. Yang, J. Feng, J. Liu, L. Sun, and W. Xu, "Flexible Optoelectronic Neural Transistors With Broadband Spectrum Sensing and Instant Electrical Processing for Multimodal Neuromorphic Computing," *SmartMat* 4, no. 2 (2023): e1154.

11. W. Li, F. Huang, C. Gao, et al., "Highly Radiation-Tolerant Polymer Field-Effect Transistors With Polystyrene Dielectric Layer," *Nano Energy* 100 (2022): 107452.

12. S. Wang, J. Xu, W. Wang, et al., "Skin Electronics From Scalable Fabrication of an Intrinsically Stretchable Transistor Array," *Nature* 555, no. 7694 (2018): 83–88.

13. H. Kwon, H. Ye, K. Shim, et al., "Newly Synthesized Nonvacuum Processed High-*K* Polymeric Dielectrics With Carboxyl Functionality for Highly Stable Operating Printed Transistor Applications," *Advanced Functional Materials* 31, no. 5 (2021): 2007304.

14. D. Ji, T. Li, Y. Zou, et al., "Copolymer Dielectrics With Balanced Chain-Packing Density and Surface Polarity for High-Performance Flexible Organic Electronics," *Nature Communications* 9 (2018): 2339.

15. H. Chen, Y. Guo, G. Yu, et al., "Highly π-Extended Copolymers With Diketopyrrolopyrrole Moieties for High-Performance Field-Effect Transistors," *Advanced Materials* 24, no. 34 (2012): 4618–4622.

16. Y. Diao, B. C. K. Tee, G. Giri, et al., "Solution Coating of Large-Area Organic Semiconductor Thin Films With Aligned Single-Crystalline Domains," *Nature Materials* 12, no. 7 (2013): 665–671.

17. Y. Liu, Y. Wei, M. Liu, et al., "Face-To-Face Growth of Wafer-Scale 2D Semiconducting Mof Films on Dielectric Substrates," *Advanced Materials* 33, no. 13 (2021): 2007741.

18. X. Yang, J. Yi, T. Wang, et al., "Wet-Adhesive On-Skin Sensors Based on Metal-Organic Frameworks for Wireless Monitoring

of Metabolites in Sweat," *Advanced Materials* 34, no. 44 (2022): 2201768.

19. R. Dong, P. Han, H. Arora, et al., "High-Mobility Band-Like Charge Transport in a Semiconducting Two-Dimensional Metal-Organic Framework," *Nature Materials* 17, no. 11 (2018): 1027–1032.

20. Y. Song, N. Xu, G. Liu, et al., "High-Yield Solar-Driven Atmospheric Water Harvesting of Metal-Organic-Framework-Derived Nanoporous Carbon With Fast-Diffusion Water Channels," *Nature Nanotechnology* 17, no. 8 (2022): 857–863.

21. L. Jiao, J. Y. R. Seow, W. S. Skinner, Z. U. Wang, and H. L. Jiang, "Metal-Organic Frameworks: Structures and Functional Applications," *Materials Today* 27 (2019): 43–68.

22. C. Xiao and Y. Xie, "The Expanding Energy Prospects of Metal Organic Frameworks," *Joule* 1, no. 1 (2017): 25–28.

23. J. F. Olorunyomi, S. T. Geh, R. A. Caruso, and C. M. Doherty, "Metal-Organic Frameworks for Chemical Sensing Devices," *Materials Horizons* 8, no. 9 (2021): 2387–2419.

24. G. Y. Qiao, S. Yuan, J. Pang, et al., "Functionalization of Zirconium-Based Metal-Organic Layers With Tailored Pore Environments for Heterogeneous Catalysis," *Angewandte Chemie International Edition* 59, no. 41 (2020): 18224–18228.

25. Z. Ji, H. Zhang, H. Liu, O. M. Yaghi, and P. Yang, "Cytoprotective Metal-Organic Frameworks for Anaerobic Bacteria," *Proceedings of the National Academy of Sciences of the United States of America* 115, no. 42 (2018): 10582–10587.

26. Y. Bai, Y. Dou, L. H. Xie, W. Rutledge, J. R. Li, and H. C. Zhou, "Zr-Based Metal-Organic Frameworks: Design, Synthesis, Structure, and Applications," *Chemical Society Reviews* 45, no. 8 (2016): 2327–2367.

27. S. Yuan, J. S. Qin, C. T. Lollar, and H. C. Zhou, "Stable Metal-Organic Frameworks With Group 4 Metals: Current Status and Trends," *ACS Central Science* 4, no. 4 (2018): 440–450.

28. D. Ji, Y. Zou, K. Wu, et al., "Highly Efficient Charge Transport in a Quasi-Monolayer Semiconductor on Pure Polymer Dielectric," *Advanced Functional Materials* 30, no. 4 (2020): 1907153.

29. J. Ma, A. G. Wong-Foy, and A. J. Matzger, "The Role of Modulators in Controlling Layer Spacings in a Tritopic Linker Based Zirconium 2D Microporous Coordination Polymer," *Inorganic Chemistry* 54, no. 10 (2015): 4591–4593.

30. X. Tang, H. Kwon, J. Hong, et al., "Direct Printing of Asymmetric Electrodes for Improving Charge Injection/Extraction in Organic Electronics," *ACS Applied Materials & Interfaces* 12, no. 30 (2020): 33999–34010.

31. Z. Peng, K. Jiang, Y. Qin, et al., "Modulation of Morphological, Mechanical, and Photovoltaic Properties of Ternary Organic Photovoltaic Blends for Optimum Operation," *Advanced Energy Materials* 11, no. 8 (2021): 2003506.

32. Z. Peng, K. Xian, Y. Cui, et al., "Thermoplastic Elastomer Tunes Phase Structure and Promotes Stretchability of High-Efficiency Organic Solar Cells," *Advanced Materials* 33, no. 49 (2021): 2106732.

33. Y. R. Shen, "Surface Properties Probed By Second-Harmonic and Sum-Frequency Generation," *Nature* 337, no. 6207 (1989): 519–525.

34. P. Balzerowski, K. Meister, J. Versluis, and H. J. Bakker, "Heterodyne-Detected Sum Frequency Generation Spectroscopy of Polyacrylic Acid at the Air/Water-Interface," *Physical Chemistry Chemical Physics* 18, no. 4 (2016): 2481–2487.

35. K. Tian, B. Zhang, S. Ye, and Y. Luo, "Intermolecular Interactions at the Interface Quantified By Surface-Sensitive Second-Order Fermi Resonant Signals," *The Journal of Physical Chemistry C* 119, no. 29 (2015): 16587–16595.

36. R. G. Snyder and J. R. Scherer, "Band Structure in the C—H Stretching Region of the Raman Spectrum of the Extended Polymethylene Chain: Influence of Fermi Resonance," *The Journal of Chemical Physics* 71, no. 8 (1979): 3221–3228.

37. S. D. Merajver, C. Lapidus, and S. L. Wunder, "Intermolecular Interactions and Fermi Resonance in Methylene Groups," *The Journal of Chemical Physics* 76, no. 6 (1982): 3344–3345.

38. R. Lu, W. Gan, B. Wu, H. Chen, and H. Wang, "Vibrational Polarization Spectroscopy of CH Stretching Modes of the Methylene Group at the Vapor/Liquid Interfaces With Sum Frequency Generation," *The Journal of Physical Chemistry B* 108, no. 22 (2004): 7297–7306.

39. H. Zhang, F. Li, Q. Xiao, and H. Lin, "Conformation of Capping Ligands on Nanoplates: Facet-Edge-Induced Disorder and Self-Assembly-Related Ordering Revealed By Sum Frequency Generation Spectroscopy," *The Journal of Physical Chemistry Letters* 6, no. 12 (2015): 2170–2176.

40. C. Lu, Y. Yang, J. Wang, et al., "High-Performance Graphdiyne-Based Electrochemical Actuators," *Nature Communications* 9, no. 1 (2018): 752.

41. W. Morris, B. Volosskiy, S. Demir, et al., "Synthesis, Structure, and Metalation of Two New Highly Porous Zirconium Metal-Organic Frameworks," *Inorganic Chemistry* 51, no. 12 (2012): 6443–6445.

42. Ş. Tokalıoğlu, E. Yavuz, S. Demir, and Ş. Patat, "Zirconium-Based Highly Porous Metal-Organic Framework (MOF-545) As an Efficient Adsorbent for Vortex Assisted-Solid Phase Extraction of Lead From Cereal, Beverage and Water Samples," *Food Chemistry* 237 (2017): 707–715.

43. J. Q. Yang, R. Wang, Y. Ren, et al., "Neuromorphic Engineering: From Biological to Spike-Based Hardware Nervous Systems," *Advanced Materials* 32, no. 52 (2020): 2003610.

44. E. Bullmore and O. Sporns, "The Economy of Brain Network Organization," *Nature Reviews Neuroscience* 13, no. 5 (2012): 336–349.

45. T. Ohno, T. Hasegawa, T. Tsuruoka, K. Terabe, J. K. Gimzewski, and M. Aono, "Short-Term Plasticity and Long-Term Potentiation Mimicked in Single Inorganic Synapses," *Nature Materials* 10, no. 8 (2011): 591–595.

46. X. Ji, B. D. Paulsen, G. K. K. Chik, et al., "Mimicking Associative Learning Using an Ion-Trapping Non-Volatile Synaptic Organic Electrochemical Transistor," *Nature Communications* 12, no. 1 (2021): 2480.

47. C. Sun, Z. Lin, W. Xu, et al., "Dipole Moment Effect of Cyano-Substituted Spirofluorenes on Charge Storage for Organic Transistor Memory," *The Journal of Physical Chemistry C* 119, no. 32 (2015): 18014–18021.

48. W. Huang, P. Hang, Y. Wang, et al., "Zero-Power Optoelectronic Synaptic Devices," *Nano Energy* 73 (2020): 104790.

49. Y. van de Burgt, E. Lubberman, E. J. Fuller, et al., "A Non-Volatile Organic Electrochemical Device As a Low-Voltage Artificial Synapse for Neuromorphic Computing," *Nature Materials* 16, no. 4 (2017): 414–418.

Supporting Information

Additional supporting information can be found online in the Supporting Information section.